PtNi bimetallic structure supported on UiO-67 metal-organic framework (MOF) during CO oxidation

Reza Vakili [a,b], Thomas J.A. Slater [c], Christopher Hardacre [a], Alex S. Walton [d,e,*], Xiaolei Fan [a,*]

[a] Department of Chemical Engineering and Analytical Science, School of Engineering, The University of Manchester, Oxford Road, Manchester M13 9PL, United Kingdom
[b] Department of Chemical Engineering, University of Bath, Claverton Down, Bath BA2 7AY, United Kingdom
[c] Electron Physical Sciences Imaging Centre, Diamond Light Source Ltd., Oxfordshire OX11 0DE, United Kingdom
[d] Department of Chemistry, School of Natural Sciences, The University of Manchester, Manchester, Oxford Road, M13 9PL, United Kingdom
[e] Photon Science Institute, The University of Manchester, Oxford Road, Manchester M13 9PL, United Kingdom

A R T I C L E   I N F O

A B S T R A C T

Supported bimetallic nanoparticles (BNPs) are promising catalysts, but study on their compositional and structural changes under reaction conditions remains a challenge. In this work, the structure of PtNi BNPs supported on UiO-67 metal–organic framework (MOF) catalyst (i.e., PtNi@UiO-67) was investigated by *in situ* by near ambient pressure X-ray photoelectron spectroscopy (NAP-XPS). The results showed differences in the reduction behaviour of Ni species in PtNi BNPs and monometallic Ni supported on UiO-67 catalysts (i.e., PtNi@UiO-67 and Ni@UiO-67), suggesting charge transfer between metallic Pt and Ni oxides in PtNi@UiO-67. Under CO oxidation conditions, Ni oxides segregated to the outer surface of the BNPs forming a thin layer of NiO_x on top of the metallic Pt (i.e., a NiO_x-on-Pt structure). This resulted in a core-shell structure which was confirmed by high-resolution scanning transmission electron microscopy (HR-STEM). Accordingly, the layer of NiO_x on PtNi BNPs, which is stabilised by charge transfer from metallic Pt, was proposed as the possible active phase for CO oxidation, being responsible for the enhanced catalytic activity observed in the bimetallic PtNi@UiO-67 catalyst.

© 2020 The Author(s). Published by Elsevier Inc. This is an open access article under the CC BY license (http://creativecommons.org/licenses/by/4.0/).

1. Introduction

Bimetallic nanoparticles (BNPs) often show different electronic and chemical properties from their monometallic parents, enabling catalysis with improved selectivity, activity and stability [1,2]. Insights into the origin of these intriguing properties have been the subject of many theoretical and experimental studies, aimed at understanding the synergy between the bimetallic phases, and thus enabling the rational design of highly active and selective catalysts based on BNPs [3–5]. For example, in catalytic oxidation of alcohols (to aldehydes) over a bimetallic AuPd/TiO2 catalyst, Au acted as an electronic promoter for Pd and improved the turnover frequency, TOF (up to 270,000 h^{-1}) and selectivity in comparison with the monometallic Au/TiO2 and Pd/TiO2 catalysts [6]. BNPs, such as PtRe and PtIr supported on Al2O3 catalysts, have gained strong commercial interest since the 1960 s for their use in hydrocarbon reforming, which has stimulated a large number of investigations on possible yet practical applications of different BNPs [7–9]. Currently, supported BNPs catalysts, composed of a transition metal (e.g., Ni, Ru and Cu) together with Pt, are widely used in, for example, oxidation [10], hydrogenation [11] and electro-catalysis (for fuel cell applications) [12]. Compared to the respective monometallic catalysts, these BNPs catalysts have more complex structures such as alloys, crystalline, Janus and core-shell arrangements. Additionally, structural variations of bimetallic phases under reaction conditions are expected to occur [13–15]. For example, dynamic variation of PtNi BNPs (supported on carbon black) under oxidising and reducing conditions was studied using *in situ* X-ray absorption spectroscopy (XAS) and X-ray diffraction (XRD). Specifically, both *in situ* techniques confirmed that, under the oxidising conditions, the outward diffusion of Ni was induced to form a NiO-rich surface on Pt phase, whereas under reducing conditions inward diffusion of Ni occurred, thus producing a Pt-rich surface [16,17]. These findings clearly show the necessity of *in situ* and *operando* studies to understand the structure-reactivity correlations in BNPs since their structures can alter significantly under reaction conditions. Over the past decades, efforts have been made to understand the nature, as well as the behaviors under reaction conditions, of such BNPs. For example, detailed X-ray absorption near edge spectroscopy (XANES) studies by Bao

---

* Corresponding authors.
E-mail addresses: alex.walton@manchester.ac.uk (A.S. Walton), xiaolei.fan@manchester.ac.uk (X. Fan).

et al. showed the formation of NiO_x-Pt(1 1 1) and NiO_x-Pt-Ni-Pt (1 1 1) surface structures in PtNi BNP catalysts supported on carbon black at reduction temperatures of 423 K and 523 K, respectively. Such ultrathin Ni oxide overlayers (NiO_x) over Pt metal, which contain coordinatively unsaturated ferrous (CUF) sites, are believed to enhance the catalytic activity of the BNPs in CO oxidation (1% CO, 20% O_2 and 79% He) [18]. Atomic layer deposition (ALD) method was employed to selectively deposit NiO_x phase on the Pt phase of model Pt supported on Al_2O_3 thin film (i.e., NiO_x/Pt/Al_2O_3), which showed comparatively high catalytic activity and thermal stability than the monometallic Pt/Al_2O_3 in CO oxidation [19]. Based on XANES characterisation, the enhanced catalytic activity was proposed to be due to the NiO_x-Pt interface created by ALD, in which NiO_x acts as the promoter. In addition to the proposed synergistic effects, the geometric and structural aspects of BNPs also play an important role in the measured improvement in activity and stability [20,21]. For example, Cheng *et al.*[22] reported a size-dependent activity in catalytic dehydrogenation of formic acid over AuPd BNPs supported on activated carbon. Specifically, TOF increased from 14 h^{-1} to 718 h^{-1} with a decrease of the size of AuPd BNPs from 12.8 ± 0.5 nm to 3.8 ± 0.5 nm.

It is known that the appropriate selection of catalyst supports (hosts) with well-defined porosity and high surface area contributes to the formation of well-dispersed small NPs (of 1–3 nm) for catalysis [23,24]. Metal-organic frameworks (MOFs) have well-defined cavities and functionalisable chemical/physical properties, which can accommodate a variety of guest species. The porous crystalline framework of MOFs can enable spatial segregation and confinement of metal NPs, and hence avoid the aggregation of NPs under reaction conditions. These features, along with the exceptionally available choices of both organic and inorganic components to construct MOFs, allow the possibility of rational design of supported catalysts on MOFs with precise control over many variables [25–27]. A recent study on monometallic Pt NPs supported on UiO-67 MOF showed that, in comparison with the conventional metal oxide supports such as ZrO_2, UiO-67 enhanced the structural confinement and limited the sintering of Pt NPs under oxidising conditions [28].

Many MOFs have been used to prepare supported BNPs due to their highly porous structures and the associated confinement effect on restricting the growth of BNPs [29–31]. For example, ultrafine AuNi BNPs with an average size of 1.8 nm were successfully immobilised on MIL-101 by a double solvent method. The resulting supported BNPs showed a high activity for hydrogen (H_2) generation from the catalytic hydrolysis of ammonia borane [32]. In addition, cascade catalysis over BNPs@MOF catalysts with three active sites (i.e., acid/base-NP_1-NP_2) has also gained interest, taking advantage of not only the synergy between BNPs but also the intrinsic active sites in MOFs [33]. For example, a PdAg@MIL-101 catalyst showed excellent catalytic activity (i.e., complete conversion) and selectivity in one-pot cascade conversion of nitroarene to the secondary arylamine. In this catalysis, MIL-101 offers Lewis acidity, Pd provides the activity for hydrogenation, and Ag increases the selectivity to the secondary arylamine [34]. Although the formation of relevant bimetallic structures in MOFs, either alloyed or core-shell, was suggested based on *ex situ* X-ray photoelectron spectroscopy (XPS) and high-resolution scanning transmission electron microscopy (HR-STEM) [35], the fundamental understanding of such bimetallic catalysts regarding their compositional and structural arrangements, especially the dynamic information of such BNPs in relation to their catalytic performance during reactions is still lacking and requires further investigation.

Herein, we present a combined near-ambient pressure (NAP)-XPS and HR-STEM study of PtNi BNPs supported on UiO-67 catalyst for CO oxidation. Specifically, XPS study was coupled with mass spectrometry (MS) to evaluate catalyst surface dynamics and

reactivity under NAP conditions. Comparative HR-STEM characterisation of the fresh and treated catalysts (under different reactive O_2 and H_2 environments) was performed to develop relevant insights into the compositional and structural variation (i.e., metal segregation) of the bimetallic phases. Findings from the NAP-XPS characterisation suggested that the NiO_x-Pt structure was the active phase, being responsible for the observed activity of CO oxidation over the supported BNPs. Under the reaction conditions used, subsurface Ni oxides segregated to the surface of the bimetallic phase, forming a thin layer of NiO_x stabilised on the Pt phase, that is, the NiO_x-on-Pt core-shell structure. This was also confirmed by HR-STEM. To the best of our knowledge, it is the first example of *operando* metal segregation observed on PtNi coreshell BNPs supported on MOF, providing an improved understanding of the compositional and structural effects of such BNPs on catalytic oxidation.

2. Experimental section

2.1. Chemicals and catalysts preparation

Zirconium (IV) chloride ($ZrCl_4$, 99.98%), platinum (II) acetylacetonate (Pt(acac)$_2$, 98%), nickel (II) acetylacetonate (Ni(acac)$_2$, 98%) and 4,4′-biphenyldicarboxylic acid (H_2BPDC, 98%) were purchased from Arcos. Benzoic acid (99.5%) was purchased from Sigma-Aldrich. *N,N*'-dimethylformamide (DMF, 99.8%) was obtained from Fischer Scientific. All chemicals were used as received, with no further purification.

UiO-67 was synthesised by a microwave-assisted method reported previously [36]. PtNi BNPs supported on UiO-67 catalyst (denoted as PtNi@UiO-67, with 1 wt% Pt and 1 wt% Ni theoretical loading) were prepared by the co-wet impregnation method. Specifically, the metal precursor solutions were prepared by dissolving 2 mg Pt(acac)$_2$ and 4.5 mg Ni(acac)$_2$ in 1 ml acetone separately and dropped on 100 mg UiO-67 MOF in tandem at room temperature (RT) to fully moisten the support with the precursor solutions. The as-synthesised catalyst was then dried in an oven at 50 °C (for 2 h) and reduced at 300 °C under H_2 (10 vol%)/Argon (Ar) flow at 70 ml min^{-1} (heating rate = 5 °C min^{-1}). Control monometallic catalysts of Pt@UiO-67 (with 2 wt% Pt) and Ni@UiO-67 (with 2 wt% Ni) catalysts were also prepared using similar protocol, as described in the Supporting Information (SI).

2.2. Characterisation of materials

X-ray diffraction (XRD) of materials was performed on a Rigaku Miniflex diffractometer using CuKα_1 radiation (λ = 0.15406 nm, 30 kV, 15 mA). The measurement was performed over a range of 4° < 2θ < 45° in 0.05 step size at a scanning rate of 1° min^{-1}. Scanning electron microscopy (SEM) was undertaken using a FEI Quanta 200 ESEM equipment using a working distance of 8–10 mm and an accelerating voltage of 20 kV. All samples were dispersed in ethanol and dropped onto SEM grids, followed by the gold coating using an Emitech K550X sputter coater at 1 × 10^{-4} mbar before SEM. Nitrogen (N_2) adsorption–desorption analysis at − 196.15 °C was carried out using a Micromeritics ASAP 2020 analyser. Prior to N_2 physisorption, samples (~100 mg) were pretreated by degassing at 200 °C under vacuum overnight. The specific surface area and total pore volume of the materials were calculated based on the Brunauer-Emmett-Teller (BET) method and at a relative pressure p/p^0 of 0.99, respectively. The quantitative determination metal loading of the catalysts was determined by inductively coupled plasma optical emission spectrometry

(ICP-OES, Thermo iCAP 6000 SERIES). Samples were digested in concentrated nitric acid overnight, and then the solutions were analysed by ICP-OES.

High resolution scanning transmission electron microscopy (HR-STEM) was performed using a JEOL ARM200F microscope in the electron Physical Sciences Imaging Centre (ePSIC) at Diamond Light Source. Three samples were prepared from the catalysis: freshly reduced PtNi@UiO-67, freshly reduced Ni@UiO-67 and used PtNi@UiO-67. All samples were sealed in an inert atmosphere immediately after the treatment. The samples were unsealed and the catalyst powder was crushed and dispersed in a dry state (to avoid any solvent-induced chemical changes to the catalysts) on to holey-carbon coated copper TEM grids (200 mesh) and were transferred into the TEM with as quickly as possible (total air exposure < 5 min). An acceleration voltage of 200 kV was used throughout the measurements. A beam current of approximately 13 pA, a convergence semi-angle of 23 mrad and a high-angle annular dark-field imaging (HAADF) inner angle of 80 mrad was used for high-resolution HAADF data. The beam current was changed to approximately 170 pA for energy-dispersive X-ray (EDX) data acquisition, which was performed using a JEOL Centurio dual-detector. EDX spectroscopic maps were extracted using full width half maximum of the $L\alpha 1$ peak of Pt and the $K\alpha 1$ peak of Ni. Radial averages were generated from Pt and Ni EDX maps by applying a circular mask to randomly selected bimetallic particles. Particles which were too close to the edge of frame or another particle were excluded from analysis. The average intensity as a function of radial distance from the centre of the particle was measured from this mask using the 'radial plot profile' plugin for the image processing software (ImageJ). The same mask with the same radial step distance was used for all particles so that the resultant radial profiled could be averaged across multiple particles.

2.3. Near ambient pressure X-ray photoelectron spectroscopy (NAP-XPS)

All XPS spectra were recorded with a SPECS NAP-XPS system employing a monochromatic Al Kα source (1486.6 eV) and a 'Devi-Sim' cell-type NAP environment attached to a SPECS Phoibos 150 NAP differentially pumped analyser. The catalyst powders were dispersed in ethanol and then drop-cast onto a gold foil substrate. The spectra were recorded at a pass energy of 30 eV and charge corrected to the main component of the C 1 s peak at 284.5 eV for aromatic carbon (the main constituent of the H_2BPDC linker in UiO-67). In situ reduction of the catalyst was performed at 1 mbar H_2 and the temperatures specified in the text (i.e., RT, 300 °C and 360 °C). Operando measurements were then performed immediately afterwards with no air exposure. Operando NAP-XPS was performed during catalyst exposure to a mixture of $CO:O_2$ (CO/O_2 ratio = 2, total pressure = 3 mbar) at RT before it was heated to 300 °C, with XPS spectra acquired at each temperature. The C 1 s and O 1 s core levels were also acquired, but for information about C and O surface species on the Pt/Ni particles could not be obtained as the signal was dominated by the C and O in the H_2BPDC linker. The acquisition time for XPS spectra at each temperature was about 2 h in the temperature-programmed measurements (at 100–300 °C). Simultaneous online gas analysis of the catalysis was monitored using a quadrupole mass spectrometer (QMS, MKS EasyView 2) in the second differential stage of the NAP hemispherical analyser. All XPS spectra were fitted using CASAXPS with a Shirley background. Symmetric Voigt profiles were used for all peaks except the metallic Pt and Ni peaks which were fitted with asymmetric Lorentzian profiles to account for their intrinsic asymmetry.

2.4. Catalysis

Catalyst light-off experiments of CO oxidation was performed in a plug-flow reactor, placed inside a programmable furnace at atmospheric pressure. The catalyst was pelletised and sieved to give particle sizes of 250–400 μm. 50 mg of the catalyst was packed into the reactor and sandwiched by quartz wool. Prior to catalysis, the catalyst was treated for at 300 °C for 1 h in a reducing environment with the H_2 (10 vol%)/Ar flow (at 100 ml min^{-1}). Previous work has shown that the condition was sufficient to fully reduce the catalyst [28]. After reduction, the reactor was firstly cooled down to RT under Ar flow (at 100 ml min^{-1}), then the temperature was ramped from RT to 410 °C at a heating rate of 6 °C min^{-1} under a reacting flow (CO/O_2 = 2, Ar as balance, total flowrate = 100 ml min^{-1}) to perform the catalysis. The bed temperature was measured by a K type thermocouple adjacent to the catalyst bed. After each run, the furnace was turned off to allow the reactor to cool down to RT under Ar (at 100 ml min^{-1}). Mass spectrometry (MS) of the outlet gas was performed using an HPR20 QIC mass spectrometer (Hiden Analytical). During the light-off experiments, the spectrometer continuously monitored the ion currents at a mass-to-charge ratio (m/e) of 36, 32, 28 and 44, corresponding to signals of Ar, O_2, CO and CO_2, respectively.

3. Results and discussions

The resulting catalysts were fully characterised using XRD, SEM and N_2 physisorption, showing that the integrity of UiO-67 framework was maintained after metal loading (Figs. S1 and S2, Table S1). ICP-OES analysis showed that the actual metal loadings match the theoretical values for all the catalysts. Comparative assessment of the catalytic activity of the catalysts was performed using CO oxidation with a stoichiometric CO/O_2 mixture (at 100 ml min^{-1}). Fig. 1a shows the comparative light-off behaviour of the catalysts under investigation. Clearly, (i) the BNP PtNi@UiO-67 catalyst demonstrated exceptionally good performance in CO oxidation in comparison to the control monometallic catalysts and, (ii) the Ni@UiO-67 catalyst was the least active one among the three catalysts under investigation. Specifically, $T_{10\%}$, $T_{50\%}$ and $T_{90\%}$ (temperatures at which CO reach 10, 50 and 90% conversion, respectively) of the BNP PtNi@UiO-67 catalyst were at 121 °C, 161 °C and 171 °C, respectively, and were much lower than that of the monometallic Pt@UiO-67 and Ni@UiO-67 catalysts (e.g., $T_{10\%}$ = 225 °C for Pt@UiO-67 and $T_{10\%}$ = 388 °C for Ni@UiO-67). The catalytic experiments were performed up to temperatures of 410 °C (at ramp rate of 6 °C min^{-1}). The monometallic Ni@UiO-67 catalyst showed incomplete CO conversion (16%) at 405 °C. Importantly, PtNi@UiO-67 also demonstrated a good stability in the cyclic deactivation tests (Fig. 1b), showing insignificant changes in $T_{10\%}$, $T_{50\%}$ and $T_{90\%}$ temperatures at 123 ± 2 °C, 164 ± 3 °C and 174 ± 3 °C, respectively, over four cycles of catalysis (as shown in Fig. S3). These results are in line with our previous findings, suggesting that the porous structure of UiO-67 MOF prevented sintering of the supported Pt NPs, and hence the anti-deactivation of the catalyst under oxidising conditions [28]. Additionally, for the BNP PtNi@UiO-67 catalyst, the metal NP mobility might also be reduced due to PtNi alloying, as reported by Colón-Mercado et al., who showed that the anchoring effect of Ni to Pt on carbon substrates (e.g., carbon black) limits the mobility of Pt NPs due to strong bonding of Pt atoms to carbon substrates through bridges of Ni atoms [37].

In order to elucidate the enhanced activity of the BNP catalyst, the surface chemistry of the Ni@UiO-67 and PtNi@UiO-67 catalysts in CO oxidation were investigated using in situ XPS under NAP conditions (CO/O_2 ratio = 2, total pressure = 3 mbar; detailed NAP-XPS
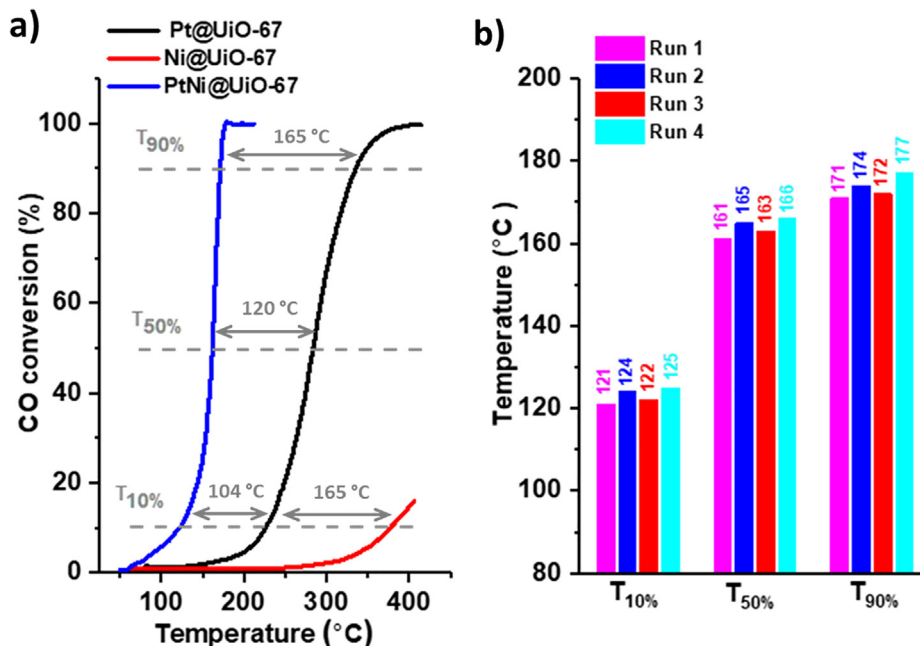
Fig. 1. (a) Comparative light-off curves of CO conversion over the monometallic and bimetallic catalysts, (b) $T_{10\%}$, $T_{50\%}$ and $T_{90\%}$ values of the BNPs PtNi@UiO-67 catalyst in the cyclic deactivation experiments (reaction conditions: heating ramp = 6 °C min^{-1}, atmospheric pressure, total flowrate = 100 ml min^{-1}, CO/O$_2$ = 2, Ar as balance).

study of CO oxidation over Pt@UiO-67 was reported in our previous work [28]). Before catalysis under the NAP conditions, the as-synthesised catalysts were reduced *in situ* under H$_2$ at 1 mbar H$_2$. Fig. 2 shows the dynamic variation of surface metallic phases in the two catalysts during reduction. For the monometallic Ni@UiO-67 catalyst, Ni 2p XPS spectra shows full reduction of the supported Ni^{2+} species to metallic Ni at 300 °C which was evidenced by the appearance of the doublet of metallic Ni (Ni 2p$_{3/2}$ at 852.5 ± 0.1 eV) at ~ 300 °C. Conversely, regarding the bimetallic PtNi@UiO-67 catalyst, annealing in H$_2$ up to 300 °C only led to the partial reduction of the Ni species (i.e., 38% metallic Ni versus 62% Ni oxides, as shown in Fig. 2b. Note: variation in spectra quality of Ni 2p region in Fig. 2 was due to the different metal loadings

in the monometallic and bimetallic catalyst). By increasing the reduction temperature further to 360 °C, only ~ 72% Ni phase was reduced (Fig. S4). The findings show that it was comparatively difficult to reduce Ni oxides in the presence of Pt species. Fig. 2c shows the full reduction of Pt species to metallic Pt at 300 °C in the BNP PtNi@UiO-67 catalyst. Interestingly, the Pt 4f$_{7/2}$ peak in the reduced bimetallic catalyst centred at a binding energy (BE) of 70.4 eV, i.e., lower than that of monometallic Pt NPs (at 71 eV) [28]. A rational explanation for the relatively low BE measured for Pt 4f in PtNi@UiO-67 could be the charge transfer between the metallic Pt and Ni oxide, suggesting an adjoining configuration of Pt metal and Ni oxide phases in the BNP catalyst, leading to the observed difficulty in reducing the Ni species. Specifically, the
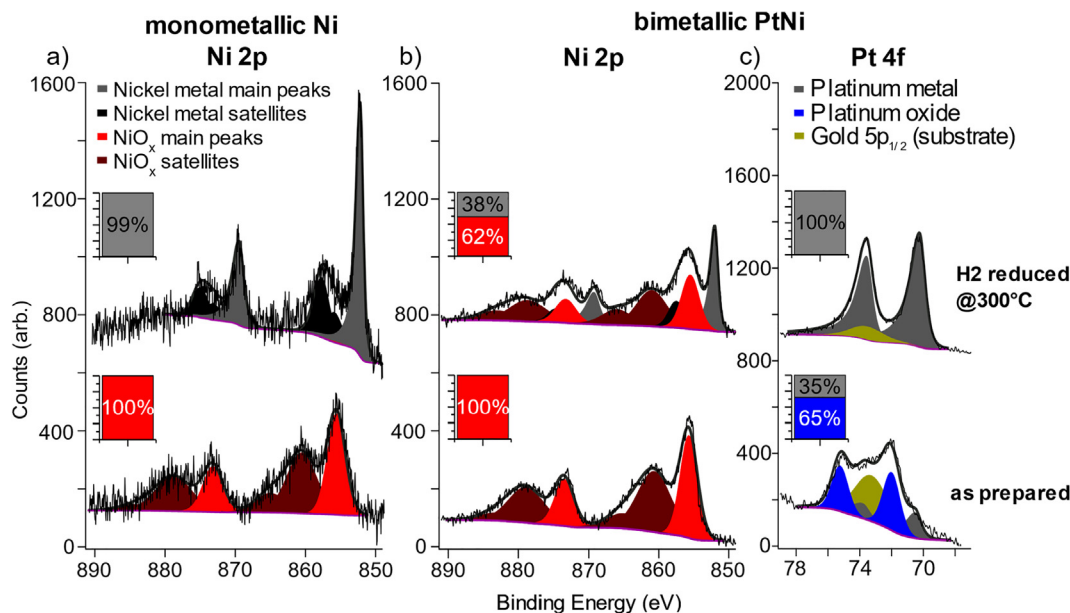

Fig. 2. NAP-XPS spectra of (a) Ni 2p of Ni@UiO-67, (b) Ni 2p of PtNi@UiO-67 and (c) Pt 4f of PtNi@UiO-6 7 at different reducing temperatures and 1 mbar H$_2$.

charge transfer between Pt and Ni stabilised a thin layer of NiO_x on top of the metallic Pt phases. Relevant charge-transfer stabilisation has been observed in model catalyst systems of 2D oxide films on single crystal metals (e.g., cobalt oxide on Au and iron oxide on Pt) [38,39]. However, such phenomena have not yet been measured for real catalysts.

During CO oxidation, under the NAP condition at a total pressure of 3 mbar ($CO/O_2 = 2$), surface dynamics of the Ni@UiO-67 and PtNi@UiO-67 catalysts were investigated by XPS coupled with simultaneous MS analysis. CO conversion data from the temperature-programmed reaction along with the corresponding XPS measurements of Pt 4f and Ni 2p regions of the catalysts are shown in Fig. 3. It should be noted that the difference between the measured CO conversions from the light-off and NAP-XPS experiments was attributed to the different configurations of the two systems, as shown previously [28]. By monitoring Ni 2p core level spectra of the reduced Ni@UiO-67 catalyst during catalysis under NAP conditions, we observed the oxidation of metallic Ni upon exposing the catalyst to the CO/O_2 mixture at 3 mbar. No CO conversion was observed at temperatures < 150 °C, while the catalytic turnover took place on active NiO surfaces at > 150 °C (Fig. 3a and 3d). When the bimetallic catalyst was exposed to the CO/O_2 mixture < 150 °C, the partially reduced Ni metal was oxidised, while metallic Pt remained under the conditions used (Fig. 3b and 3c). A previous study on supported Pt NPs on UiO-67

MOF showed a BE shift of Pt $4f_{7/2}$ from 71.2 eV (metallic state) to 71.8 eV due to the adsorption of CO on metallic Pt surfaces at relatively low temperatures (<200 °C) [28]. One explanation as to why the phenomenon did not occur in the bimetallic catalyst might be attributed to the passivation of Pt metals by a layer of NiO_x, suggesting a core-shell structure for the PtNi BNPs under the conditions used. In this case, Pt metal mostly diffuses into the core of the BNPs while NiO_x segregates to the surface of the BNPs due to the lower surface energy of Ni oxides than that of Pt metal. Previously, metal oxide-Pt interfaces of BNPs, such as FeO_x-Pt(1 1 1) [40] and NiO_x-Pt interface [19] structures, were proposed as the active phases for CO oxidation. Additionally, herein, based on the findings from the NAP-XPS analysis, we also propose that the NiO_x ultrathin layer stabilised on the metallic Pt was the possible active phase responsible for the active bimetallic PtNi@UiO-67 catalyst (Fig. 3b and 3c) in comparison with the bulk NiO in the monometallic Ni@UiO-67 catalyst (Fig. 3a). Density functional theory (DFT) calculations on different PtNi model structures (i.e., NiO_x-Pt, Pt(1 1 1) and NiO/Pt) showed that the activation energy barrier (E_a) of CO oxidation over the NiO_x-Pt model structure was the lowest (0.37 eV) in comparison with others (i.e., 0.86 eV for Pt(1 1 1) and 1.08 eV for NiO/Pt, respectively) [41], supporting the experimental findings by this work (Fig. 1a and Fig. 3d).

To confirm the hypothesis derived from the NAP-XPS study of CO oxidation over the catalysts, we performed HR-STEM analysis
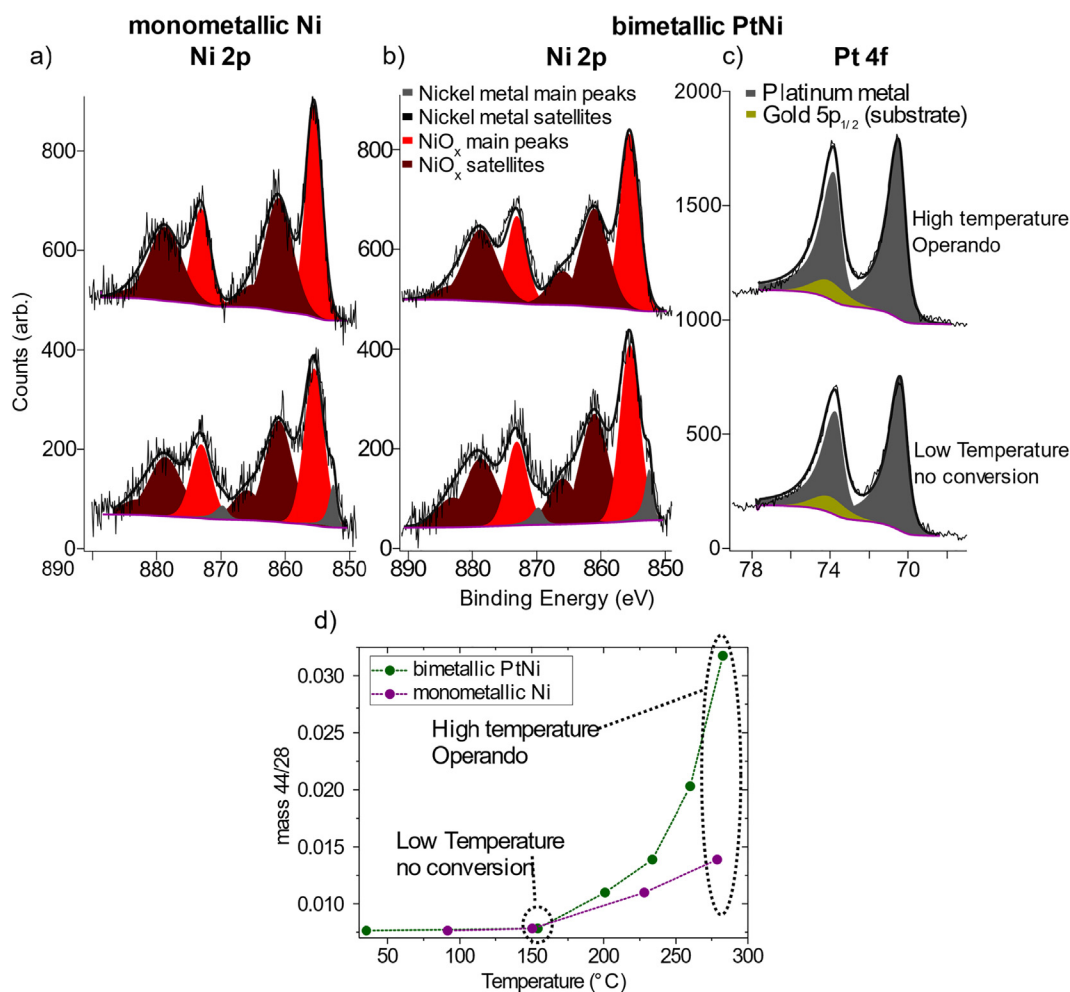

Fig. 3. Temperature programmed CO oxidation over the Ni@UiO-67 and PtNi@UiO-67 catalysts under NAP-XPS conditions (CO/O_2 ratio = 2, total pressure = 3 mbar): (a) Ni 2p spectra of Ni@UiO-67, (b) Ni 2p spectra of PtNi@UiO-67, (c) Pt 4f spectra of PtNi@UiO-67; and (d) CO conversion by MS for the monometallic and bimetallic catalysts at different reaction temperatures.

on three exemplar catalysts. The as-reduced monometallic Ni@UiO-67, as-reduced BNPs Ni/Pt@UiO-67 and used BNPs PtNi@UiO-67 (from the catalysis under the plug-flow conditions) were all imaged, and the results are shown in Fig. 4. Fig. 4a (i.e., HAADF images of the samples) confirms that, for the as-reduced catalysts under investigation (i.e., the fresh catalysts), (i) metal NPs are incorporated within the MOF matrix and (ii) the distribution of metal NPs throughout the individual MOF particle appears to be uniform. High magnification images of the monometallic Ni NPs show that they are relatively large, polycrystalline particles with a diameter of > 10 nm. Lattice resolution images show a characteristic fringe spacing of 2.02 ± 0.08 Å (average of 8 measurements on 8 different particles), which is consistent with the (2 0 0) plane in rock-salt NiO [42]. In contrast, the BNPs supported on UiO-67 show a very different morphology (Fig. 4c and 4d), with much smaller particles at ~ 2 nm, which appear to be single crystalline and have remarkable monodispersity. Lattice resolution images show a characteristic spacing of 2.33 ± 0.07 Å, which is consistent with (1 1 1) planes in metallic Pt [43]. There were no apparent differences in the morphology or crystal structure observed between the freshly reduced (Fig. 4c) and used (Fig. 4d) PtNi@UiO-67 catalysts. A more comprehensive set of HAADF images for the three catalyst samples studies is shown in Fig. S5.

EDX spectroscopic maps were taken of small groups of the freshly reduced PtNi@UiO-67. A representative set of maps is shown in Fig. 4e (four more maps are shown in Fig. S6). The maps of the Pt Lα and Ni Kα peaks confirm that Ni and Pt are co-located within single particles and the overlay image is suggestive of a core-shell structure (the Ni maps are in general more diffuse and larger in spatial extent for a given particle), confirming the hypothesis proposed according to the findings from the NAP-XPS characterisation. Furthermore, comparative EDX spectra formed by averaging over an entire particle (64 pixels) and the same size area from a section of MOF (where there are no metal particles) confirm that there is no detectible Ni or Pt dispersed on the MOF matrix, i.e. it is all localised in the particles (Fig. S7).

To further confirm the proposed core-shell NiO$_x$-Pt structure within the MOF matrix, radial averages of 18 particles were taken for both the Pt and Ni EDX maps. A radial average displays normalised counts from the centre of the particle to its surface, taking in to account all pixels within the particle (a radial profile begins in the centre of the particle, stepping out incrementally pixel-by-pixel and taking the average intensity of all pixels at a certain radius. A further description of the method is described elsewhere [44]).

The expected behaviour for a radial average of a core-shell particle is that the core element will decay smoothly from the central
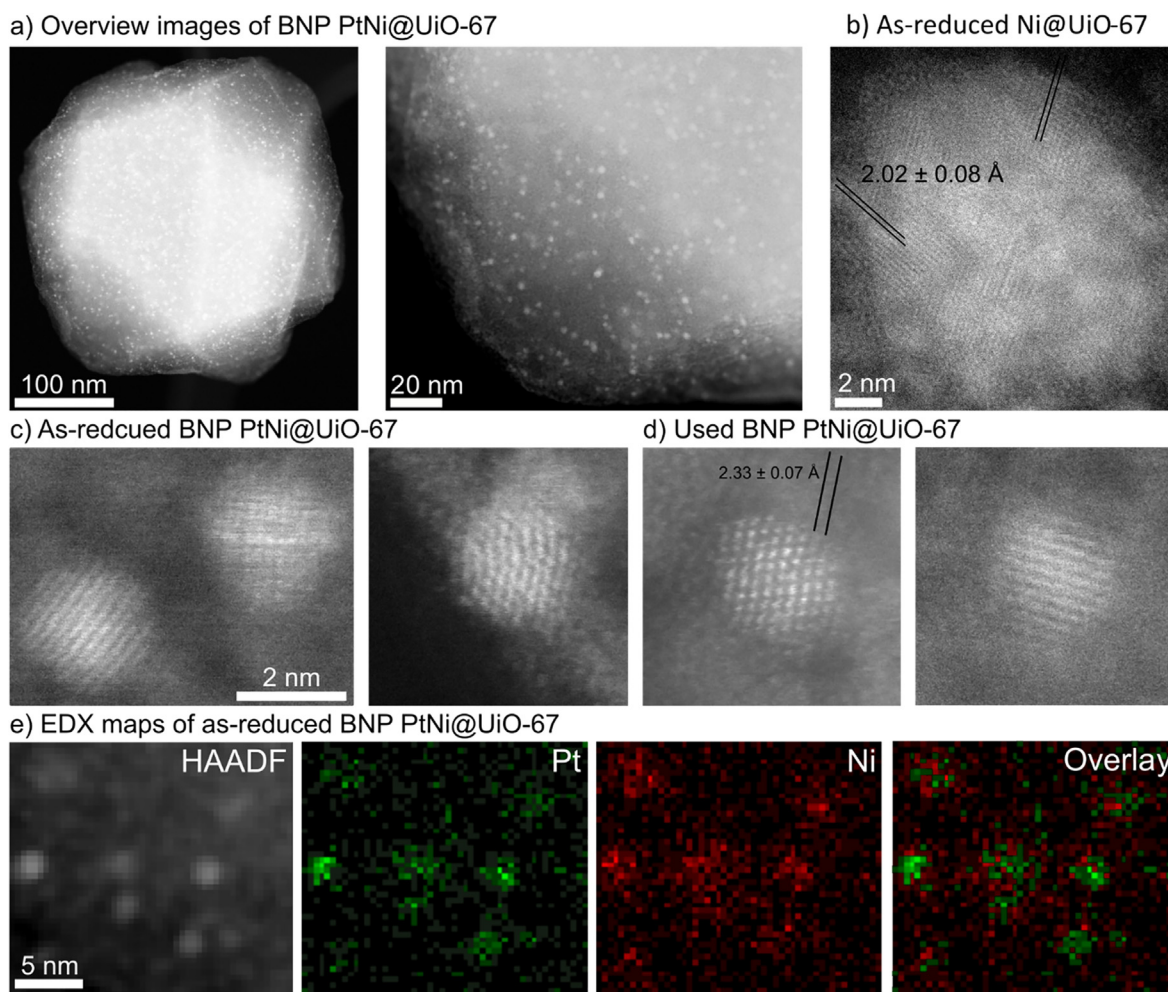
Fig. 4. STEM images: (a) HAADF images of the fresh PtNi@UiO-67 catalyst at low magnification showing a single UiO-67 particle (hosting the metal NPs) and a higher magnification image showing individual PtNi BNPs within the MOF; (b) lattice resolution HAADF image of a freshly reduced monometallic Ni catalyst particle; (c) lattice resolution HAADF images of freshly reduced PtNi BNPs – scale the same for all four images; (d) lattice resolution HAADF images of used PtNi BNPs; and (e) EDX maps of freshly reduced PtNi BNPs supported on UiO-67 MOF, showing distribution of Pt and Ni phase in the matrix of the MOF.

position and the shell element will display a more complex structure with a plateau in the central region and a maximum further out (where the electron beam is going solely through the shell and not the core) [45]. An example of a radial average from a single particle which shows this behaviour very clearly is seen in Fig. 5a. To confirm that this core-shell structure is present in most if not all particles, the radial averages from 18 different particles were combined in Fig. 5b, where the averaged trace also shows the characteristic core-shell behaviour. The radial averages suggest that the NiO_x shell thickness is extremely thin, i.e., <5 Å, which may explain why no shell is clearly discernible on the Pt cores in the HAADF images (Fig. 4c and 4d), in addition to the fact that Ni and O have a much lower atomic number than Pt and so will be of much lower intensity in the HAADF images. Regarding the probe size of STEM, it was approximately 1 Å full width half maximum before interaction with the sample. However, beam broadening due to scattering through the support material could increase this size considerably. In the centre of the MOF particles, the electron beam might pass through approximately 200 nm of UiO-67, which could result in beam broadening so that 90% of the probe was contained in a circle of diameter of approximately 5.4 nm at the exit surface of the MOF particle [46]. The average width of the beam through the sample at the centre point was therefore approximately 2 nm [46]. At the edge of the MOF particle, where the data were collected, beam broadening was substantially lower due to the relatively low thickness of the MOF. We cannot accurately determine the probe

diameter at all points but note that atomic columns could be observed in the ADF images of all particles imaged, which would place a maximum on the probe diameter of approximately 2 Å. This is approximately equivalent to the pixel size used in the EDX maps, which will have a resolution of 2–3 times the pixel size (approximately 5 Å).

Accordingly, combining the findings from the HR-STEM and NAP-XPS analyses, we propose that the *operando* surface structure is a charge-transfer stabilised NiO_x monolayer over a Pt metallic core, much like the charge transfer stabilised films of FeO and CoO which have been observed on single crystals [38,39]. More importantly, in contrast to the results of Mu *et al.* [18], we found that under *operando* conditions the metals are fully phase-separated, i.e., no metallic Ni remains alloyed with the Pt core, and this was evidenced by the absence of a metallic Ni peak during the XPS analysis of the catalyst under the *operando* conditions. It also worth noting that it is generally accepted that the structural variation and the formation of the thermodynamically stable structures in bimetallic phases are related to the chemical environment present on the surface. Density functional theory (DFT) calculations, as well as experimental results, of the bimetallic Pt-M catalysts shows that M−Pt−Pt (M represents Ni, Co and Fe) is the most thermodynamically stable structure under the oxidising environment due to the lower surface energy of transition metals than that of Pt metal (i.e., thermodynamic potential for segregation, ΔE_{seg}, is negative) [47,48]. Accordingly, NiO_x segregates on Pt metal surface can be attributed to the Ni-Pt-Pt structure, which is thermodynamically preferred configuration in the PtNi@UiO-67 catalyst under the conditions used in this work.

4. Conclusions

Understanding the behaviour of bimetallic nanoparticles (BNPs) under reaction conditions is crucial to progress the development and application of these catalysts. Herein, a well-dispersed PtNi BNPs supported on UiO-67 catalyst was prepared (i.e., PtNi@UiO-67) and studied to gain insight into its intrinsic structural and catalytic properties. Comparative light-off experiments of catalytic CO oxidation were performed over the PtNi@UiO-67 and monometallic control catalysts (i.e., Pt@UiO-67 and Ni@UiO-67), which showed the synergistic effect of PtNi BNPs through a much improved catalytic activity in comparison with the control (e.g., $T_{10\%}$ = 121 °C for PtNi@UiO-67 versus $T_{10\%}$ = 225 °C and 388 °C for Pt@UiO-67 and Ni@UiO-67, respectively). Under reducing conditions (1 mbar H_2), NAP-XPS characterisation revealed (i) the resistance of NiO_x phase to reduction for the bimetallic particle compared with monometallic system and (ii) the anomalously low binding energy of Pt 4f in PtNi@UiO-67, which suggested a core-shell bimetallic configuration and stabilisation of the NiO_x phase by Pt via charge transfer. The NiO_x shell-metallic Pt core structure of the supported BNPs was then confirmed by comprehensive post-mortem HR-STEM analysis. Accordingly, based on the findings, it was proposed that the stabilised shell NiO_x phase in PtNi@UiO-67 is responsible for the measured improvement in its catalytic activity in CO oxidation. It is worth mentioning that we cannot rule out interfacial sites existing (as the current techniques employed cannot determine whether the NiO_x shell was complete or not), and they may indeed also be active. Accordingly, further investigation to gain the insight into this aspect is needed.

Declaration of Competing Interest

The authors declare that they have no known competing financial interests or personal relationships that could have appeared to influence the work reported in this paper.
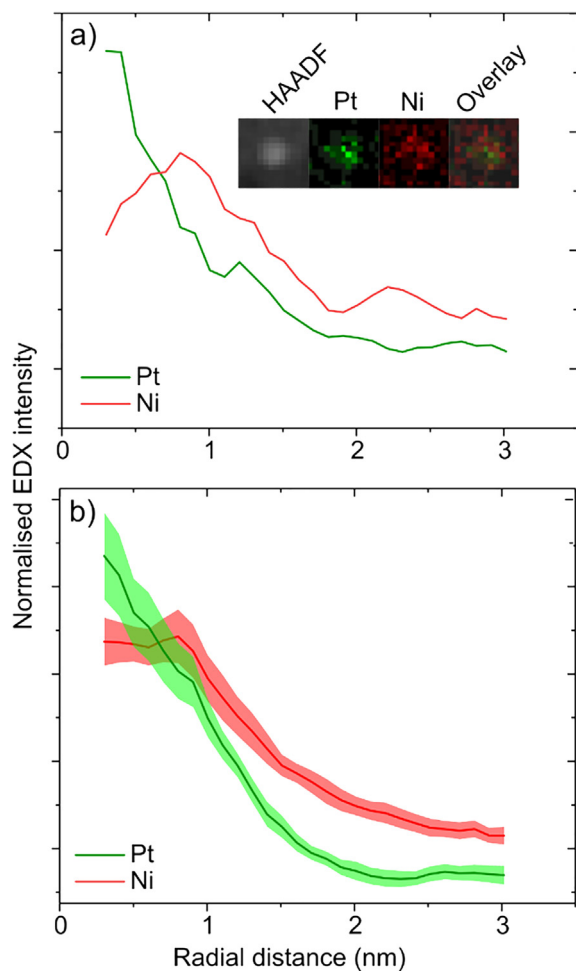
Fig. 5. (a) Radial average of a single particle from the Pt and Ni EDX maps, showing the core-shell structure. (b) Averaged traces from 18 randomly selected bimetallic particles from the freshly reduced catalyst.

Acknowledgements

References

[1] R. Ferrando, J. Jellinek, R.L. Johnston, Nanoalloys: from theory to applications of alloy clusters and nanoparticles, Chem. Rev. 108 (2008) 846–910.

[2] M. Chen, D. Kumar, C.-W. Yi, D.W. Goodman, The promotional effect of gold in catalysis by palladium-gold, Science 310 (2005) 291–293.

[3] X. Liu, A. Wang, L. Li, T. Zhang, C.-Y. Mou, J.-F. Lee, Structural changes of Au–Cu bimetallic catalysts in CO oxidation: In situ XRD EPR, XANES, and FT-IR characterizations, J. Catal. 278 (2011) 288–296.

[4] A.K. Singh, Q. Xu, Synergistic catalysis over bimetallic alloy nanoparticles, ChemCatChem 5 (2013) 652–676.

[5] J.A. Rodriguez, D.W. Goodman, The nature of the metal-metal bond in bimetallic surfaces, Science 257 (1992) 897–903.

[6] D.I. Enache, J.K. Edwards, P. Landon, B. Solsona-Espriu, A.F. Carley, A.A. Herzing, M. Watanabe, C.J. Kiely, D.W. Knight, G.J. Hutchings, Solvent-free oxidation of primary alcohols to aldehydes using Au-Pd/TiO2 catalysts, Science 311 (2006) 362–1264.

[7] J.L. Carter, G.B.M. Vicker, W. Weissman, W.S. Kmak, J.H. Sinfelt, Bimetallic catalysis: Application in catalytic reforming, Applied Catalysis 3 (1982) 321–346.

[8] Z. Bian, S. Das, M.H. Wai, P. Hongmanorom, S. Kawi, A Review on Bimetallic Nickel-Based Catalysts for CO2 Reforming of Methane, Chemphyschem European J. Chem. Phys. Phys. Chem. 18 (2017) 3117–3134.

[9] F.F. Tao, Synthesis, catalysis, surface chemistry and structure of bimetallic nanocatalysts, Chem. Soc. Rev. 41 (2012) 7977–7979.

[10] S. Alayoglu, A.U. Nilekar, M. Mavrikakis, B. Eichhorn, Ru-Pt core-shell nanoparticles for preferential oxidation of carbon monoxide in hydrogen, Nat. Mater. 7 (2008) 333–338.

[11] L.E. Murillo, A.M. Goda, J.G. Chen, Selective hydrogenation of the CdO bond in acrolein through the architecture of bimetallic surface structures, J. American Chem. Soc. 129 (2007) 7101–7105.

[12] P. Strasser, S. Koh, T. Anniyev, J. Greeley, K. More, C. Yu, Z. Liu, S. Kaya, D. Nordlund, H. Ogasawara, M.F. Toney, A. Nilsson, Lattice-strain control of the activity in dealloyed core–shell fuel cell catalysts, Nat. Chem. 2 (2010) 454–460.

[13] F. Tao, M.E. Grass, Y. Zhang, D.R. Butcher, J.R. Renzas, Z. Liu, J.Y. Chung, B.S. Mun, M. Salmeron, G.A. Somorjai, Reaction-driven restructuring of Rh-Pd and Pt-Pd core-shell nanoparticles, Science 322 (2008) 932–934.

[14] M. Sankar, N. Dimitratos, P.J. Miedziak, P.P. Wells, C.J. Kiely, G.J. Hutchings, Designing bimetallic catalysts for a green and sustainable future, Chem. Soc. Rev. 41 (2012) 8099–8139.

[15] W. Yu, M.D. Porosoff, J.G. Chen, Review of Pt-based bimetallic catalysis: from model surfaces to supported catalysts, Chem. Rev. 112 (2012) 5780–5817.

[16] R. Mu, Q. Fu, H. Liu, D. Tan, R. Zhai, X. Bao, Reversible surface structural changes in Pt-based bimetallic nanoparticles during oxidation and reduction cycles, Appl. Surf. Sci. 255 (2009) 7296–7301.

[17] R. Mu, X. Guo, Q. Fu, X. Bao, Oscillation of Surface Structure and Reactivity of PtNi Bimetallic Catalysts with Redox Treatments at Variable Temperatures, J. Phys. Chem. C 115 (2011) 20590–20595.

[18] R. Mu, Q. Fu, H. Xu, H. Zhang, Y. Huang, Z. Jiang, S. Zhang, D. Tan, X. Bao, Synergetic effect of surface and subsurface Ni species at Pt-Ni bimetallic catalysts for CO oxidation, J. American Chem. Soc. 133 (2011) 1978–1986.

[19] J. Cai, J. Zhang, K. Cao, M. Gong, Y. Lang, X. Liu, S. Chu, R. Shan, R. Chen, Selective Passivation of Pt Nanoparticles with Enhanced Sintering Resistance and Activity toward CO Oxidation via Atomic Layer Deposition, ACS Appl. Nano Mater. 1 (2018) 522–530.

[20] J. Kugai, V. Subramani, C. Song, M. Engelhard, Y. Chin, Effects of nanocrystalline CeO2 supports on the properties and performance of Ni–Rh bimetallic catalyst for oxidative steam reforming of ethanol, J. Catal. 238 (2006) 430–440.

[21] B. Coq, F. Figueras, Structure–activity relationships in catalysis by metals: some aspects of particle size, bimetallic and supports effect, Coord. Chem. Rev. 178–180 (1998) 1753–1783.

[22] J. Cheng, X. Gu, X. Sheng, P. Liu, H. Su, Exceptional size-dependent catalytic activity enhancement in the room-temperature hydrogen generation from formic acid over bimetallic nanoparticles supported by porous carbon, J. Mater. Chem. A 4 (2016) 1887–1894.

[23] G.C. Bond, The origins of particle size effects in heterogeneous catalysis, Surf. Sci. 156 (1985) 966–981.

[24] D.L. Trimm, A. Stanislaus, The control of pore size in alumoina catalyst supports: A review, Appl. Catal. 21 (1986) 215–238.

[25] H. Furukawa, K.E. Cordova, M. O'Keeffe, O.M. Yaghi, The chemistry and applications of metal-organic frameworks, Science 341 (2013) 1230444.

[26] A. Dhakshinamoorthy, H. Garcia, Catalysis by metal nanoparticles embedded on metal-organic frameworks, Chem. Soc. Rev. 41 (2012) 5262–5284.

[27] J. Liu, L. Chen, H. Cui, J. Zhang, L. Zhang, C.Y. Su, Applications of metal-organic frameworks in heterogeneous supramolecular catalysis, Chem. Soc. Rev. 43 (2014) 6011–6061.

[28] R. Vakili, E.K. Gibson, S. Chansai, S. Xu, N. Al-Janabi, P.P. Wells, C. Hardacre, A. Walton, X. Fan, Understanding the CO oxidation on Pt nanoparticles supported on MOFs by operando XPS, ChemCatChem 10 (2018) 4238–4242.

[29] Y.Z. Chen, Q. Xu, S.H. Yu, H.L. Jiang, Tiny Pd@Co core-shell nanoparticles confined inside a metal-organic framework for highly efficient catalysis, Small 11 (2015) 71–76.

[30] Y.Z. Chen, B. Gu, T. Uchida, J. Liu, X. Liu, B.J. Ye, Q. Xu, H.L. Jiang, Location determination of metal nanoparticles relative to a metal-organic framework, Nat. Commun. 10 (2019) 3462.

[31] L. Chen, X. Chen, H. Liu, Y. Li, Encapsulation of Mono- or Bimetal Nanoparticles Inside Metal-Organic Frameworks via In situ Incorporation of Metal Precursors, Small 11 (2015) 2642–2648.

[32] Q.L. Zhu, J. Li, Q. Xu, Immobilizing metal nanoparticles to metal-organic frameworks with size and location control for optimizing catalytic performance, J. American Chem. Soc. 135 (2013) 10210–10213.

[33] Q. Wang, D. Astruc, State of the Art and Prospects in Metal-Organic Framework (MOF)-Based and MOF-Derived Nanocatalysis, Chem. Rev. 120 (2020) 1438–1511.

[34] Y.-Z. Chen, Y.-X. Zhou, H. Wang, J. Lu, T. Uchida, Q. Xu, S.-H. Yu, H.-L. Jiang, Multifunctional PdAg@MIL-101 for One-Pot Cascade Reactions: Combination of Host-Guest Cooperation and Bimetallic Synergy in Catalysis, ACS Catal. 5 (2015) 2062–2069.

[35] L. Chen, B. Huang, X. Qiu, X. Wang, R. Luque, Y. Li, Seed-mediated growth of MOF-encapsulated Pd@Ag core-shell nanoparticles: toward advanced room temperature nanocatalysts, Chem. Sci. 7 (2016) 228–233.

[36] R. Vakili, S. Xu, N. Al-Janabi, P. Gorgojo, S.M. Holmes, X. Fan, Microwave-assisted synthesis of zirconium-based metal organic frameworks (MOFs): Optimization and gas adsorption, Micropor. Mesopor. Mater. 260 (2018) 45–53.

[37] H.R. Colón-Mercado, H. Kim, B.N. Popov, Durability study of Pt3Ni1 catalysts as cathode in PEM fuel cells, Electrochem. Commun. 6 (2004) 795–799.

[38] L. Giordano, M. Lewandowski, I.M.N. Groot, Y.N. Sun, J. Goniakowski, C. Noguera, S. Shaikhutdinov, G. Pacchioni, H.J. Freund, Oxygen-Induced Transformations of an FeO(111) Film on Pt(111): A Combined DFT and STM Study, J. Phys. Chem. C 114 (2010) 21504–21509.

[39] A.S. Walton, J. Fester, M. Bajdich, M.A. Arman, J. Osiecki, J. Knudsen, A. Vojvodic, J.V. Lauritsen, Interface Controlled Oxidation States in Layered Cobalt Oxide Nanoislands on Gold, ACS Nano 9 (2015) 2445–2453.

[40] Q. Fu, W.X. Li, Y. Yao, H. Liu, H.Y. Su, D. Ma, X.K. Gu, L. Chen, Z. Wang, H. Zhang, B. Wang, X. Bao, Interface-confined ferrous centers for catalytic oxidation, Science 328 (2010) 1141–1144.

[41] J. Kim, W.H. Park, W.H. Doh, S.W. Lee, M.C. Noh, J.-J. Gallet, F. Bournel, H. Kondoh, K. Mase, Y. Jung, B.S. Mun, J.Y. Park, Adsorbate-driven reactive interfacial Pt-NiO$_{1-x}$ nanostructure formation on the Pt3Ni(111) alloy surface, Sci. Adv. 4 (2018) 1–7.

[42] K. Koga, M. Hirasawa, Gas-phase generation of noble metal-tipped NiO nanorods by rapid thermal oxidation, Mater. Res. Exp. 1 (2014) 045021.

[43] J. Wu, S. Helveg, S. Ullmann, Z. Peng, A.T. Bell, Growth of encapsulating carbon on supported Pt nanoparticles studied by in situ TEM, J. Catal. 338 (2016) 295–304.

[44] Y.C. Wang, T.J.A. Slater, T.S. Rodrigues, P.H.C. Camargo, S.J. Haigh, Automated quantification of morphology and chemistry from STEM data of individual nanoparticles, J. Phys. Conf. Ser. 902 (2017) 012018.

[45] T.J.A. Slater, A. Macedo, S.L.M. Schroeder, M.G. Burke, P. O'Brien, P.H.C. Camargo, S.J. Haigh, Correlating Catalytic Activity of Ag–Au Nanoparticles with 3D Compositional Variations, Nano Lett. 14 (2014) 1921–1926.

[46] D.B. Williams, J.R. Michael, J.I. Goldstein, A.D. Romig, Definition of the spatial resolution of X-ray microanalysis in thin foils, Ultramicroscopy 47 (1992) 121–132.

[47] C.A. Menning, J.G. Chen, General trend for adsorbate-induced segregation of subsurface metal atoms in bimetallic surfaces, J. Chem. Phys. 130 (2009) 1–7.

[48] C.A. Menning, J.G. Chen, Regenerating Pt–3d–Pt model electrocatalysts through oxidation–reduction cycles monitored at atmospheric pressure, J. Power Sour. 195 (2010) 3140–3144.